Received 9 December 2023; revised 24 January 2024; accepted 27 January 2024. Date of publication 30 January 2024; date of current version 26 March 2024.

*Digital Object Identifier 10.1109/OJAP.2024.3360292*

# The Effective Number of Degrees of Freedom of the Far-Fields Radiated by Rectangular Current Sheets

**TING ZANG (Graduate Student Member, IEEE), AND GAOBIAO XIAO (Senior Member, IEEE)**

State Key Laboratory of Radio Frequency Heterogeneous Integration, Shanghai Jiao Tong University, Shanghai 200240, China

CORRESPONDING AUTHOR: G. XIAO (e-mail: gaobiaoxiao@sjtu.edu.cn)

This work was supported in part by the National Key Research and Development Program of China under Grant 2019YFB2204703, and in part by the National Natural Science Foundation of China under Grant 62188102.

**ABSTRACT** The number of degrees of freedom (NDF) of the electromagnetic far-fields generated by current sheets under certain noise level in the environment is evaluated numerically by directly sampling on the constellation of the propagation modes in free space. The electric fields in the far region are efficiently calculated by using the far-field approximation, and the effective numbers of degrees of freedom (ENDFs) are obtained through singular value decomposition (SVD) incorporating noises. The results show that ENDF is proportional to the area of the current sheets. Due to the effect of noise, when two current sheets in parallel are closer within a threshold, the differential mode fields will be submerged by the noise, so the ENDF is only determined by the common modes. Although the threshold is signal-to-noise ratio (SNR) dependent, the ENDF provides a clear physical meaning. When two current sheets are located in the same plane, numerical results suggest that the ENDF is mainly determined by the total area of the two current sheets, and the spacing between them almost does not affect the ENDF.

**INDEX TERMS** Effective number of degrees of freedom, electromagnetic far field, singular value decomposition, signal-to-noise ratio.

## I. INTRODUCTION

THE NUMBER of degrees of freedom (NDF) of an electro- magnetic field is commonly defined as the minimum number of linear independent parameters required to describe the state of the field under a given accuracy. The concept of the NDF holds significant importance across multiple research domains. It finds applications in various areas such as applied electromagnetic field problems, including antenna array synthesis [1], antenna measurement [2], and radar cross section evaluation [3]. NDF is essential in reconstruction problems, encompassing electromagnetic inverse source problems [4], [5], [6] and electromagnetic inverse scattering problems [7], [8], [9]. Furthermore, NDF is crucial in channel evaluation for wireless communication [10], [11], [12], [13], particularly in identifying channels that can effectively transmit information, especially in the multiple-input multiple-output (MIMO) systems. The study of NDF plays a crucial role in understanding system behavior, optimizing performance, and designing efficient algorithms.

The NDF of electromagnetic systems have been extensively investigated in optical imaging applications [14], [15]. More recently, there has been significant research focusing on the NDF of systems with potential applications in multi-antenna wireless communications [16], [17]. By understanding the NDF, researchers can assess the system's potential for achieving high data rates, mitigating interference, and enhancing overall performance. However, most of them mainly consider the NDF of channels from the perspective of communication, rarely from field perspectives, and might possibly overlook the nature of the electromagnetic fields themselves. In fact, the limit of information transmission is dictated by the amount of information that an electromagnetic field is capable of carrying [18]. The study of the NDF from electromagnetic field perspectives provides a better understanding of the essence of information transmission.

The NDF, as defined in [19], was utilized by Hanlen and Fu [20] for assessing communication modes in the presence of reflecting plane scatterers. An extension by Xu

and Janaswamy [21] introduced a noise-dependent definition to determine the NDF based on analyzing multiple scattering effects. Following Xu et al.'s concept, our study aims to explore the quantitative and qualitative characteristics of the ENDF associated with the far-field radiated by current sheets. In this paper, the ENDF is defined as the count of the modes excited above the noise level in the far-fields.

Unlike previous works, our study focuses on the ENDF of the far-fields associated with the sources on the plates in free space. Two models are mainly involved in this paper: a single-layer current sheet model and a double-layer current sheets model. The single-layer model is reasonable for modeling planar antenna arrays with symmetrical radiation patterns [22], [23], while the double-layer current sheets model is applicable for planar arrays with non-symmetrical radiation patterns [24]. We start directly from the expression of the radiation far-fields generated by the current sources. By incorporating the properties of model fields as prior knowledge, we directly sample on the peak directions of the propagation modes which referred to as the constellation in this paper. After obtaining the far-fields, SVD is employed to analyze and determine the ENDF.

The paper is organized as follows. The mathematical formulation of the ENDF of far-fields is presented in Section II. The ENDF of far-fields of current sheets is discussed in Section III, including three specific cases. Finally, Section IV, the concluding remarks are summarized.

## II. MATHEMATICAL FORMULATION

Planar arrays are commonly employed in 5G/6G systems. And planar structures are also commonly used in intelligent meta-surfaces. Therefore, we focus on the ENDF of the far-field of the current sheets with planar structures.

While the derivation process remains consistent with prior works [22], [23], [24], we briefly review the derivation process for the convenience of readers' understanding. In free space, the electric field $\mathbf{E}$ at position $\mathbf{r}$ of a current source $\mathbf{J}(\mathbf{r})$ in source region $V_s$ can be generally expressed as:

$$\mathbf{E}(\mathbf{r}) = -j\omega\mu_0\left(\bar{\mathbf{I}} - \hat{\mathbf{a}}_r\hat{\mathbf{a}}_r\right)\cdot\frac{e^{-\mathrm{j}kr}}{4\pi r}\int_{V_s} e^{j\mathbf{k}\cdot\mathbf{r}'}\mathbf{J}(\mathbf{r}')d\mathbf{r}' \quad (1)$$

where $\mathbf{k} = k_x\hat{\mathbf{a}}_x + k_y\hat{\mathbf{a}}_y + k_z\hat{\mathbf{a}}_z$ is the wavevector, $\hat{\mathbf{a}}_r$is the radial unit vector, and $\bar{\mathbf{I}}$ is the identity operator.

Consider a current source on a rectangular sheet in the $xoy$ plane with a size of $D_x \times D_y$, centering at origin, as shown in Fig. 1(a). By using the far-field approximation, its far field normalized with $(-\frac{4\pi re^{jk_0r}}{j\omega\mu_0})$ can be separated into two polarizations,

$$\begin{aligned}\mathbf{F}(\theta,\varphi) = {} & \sin\theta_x\hat{\boldsymbol{\theta}}_x\int_{-\frac{D_y}{2}}^{\frac{D_y}{2}}\int_{-\frac{D_x}{2}}^{\frac{D_x}{2}} e^{jk_xx+jk_yy}e^{jk_zd}I_x(x,y)dxdy \\ & + \sin\theta_y\hat{\boldsymbol{\theta}}_y\int_{-\frac{D_y}{2}}^{\frac{D_y}{2}}\int_{-\frac{D_x}{2}}^{\frac{D_x}{2}} e^{jk_xx+jk_yy}e^{jk_zd}I_y(x,y)dxdy \quad (2)\end{aligned}$$

where $k_x = k\sin\theta\cos\varphi\theta_x$, $k_y = k\sin\theta\sin\varphi$. $\theta_x$ is the angle between the position vector $\mathbf{r}$ and the $x$-axis, and $\theta_y$ is that

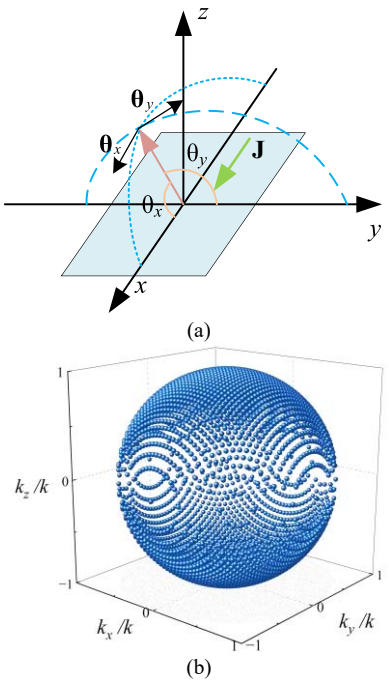


**FIGURE 1.** Current sheet. (a) The unit vectors in the coordinate system. (b) Constellation of the propagation group in the *k*-space.

with the $y$-axis. $\hat{\boldsymbol{\theta}}_x$ and $\hat{\boldsymbol{\theta}}_y$ are the corresponding unit vectors, respectively, as shown in Fig. 1(a). We choose $D_x = N_x\lambda$, $D_y = N_y\lambda$. $\lambda$ is the wavelength. $N_x$ and $N_y$ are integers. Taking the $x$-polarization as an example, the planar current is expanded with 2-D Fourier series,

$$I_x(x,y) = \sum_{m=-\infty}^{\infty}\sum_{n=-\infty}^{\infty} I_{xmn}e^{j(m\Omega_xx+n\Omega_yy)} \quad (3)$$

and its far-field can be expressed as

$$F_x(\theta,\varphi) = D_xD_y\sin\theta_x\sum_{m=-\infty}^{\infty}\sum_{n=-\infty}^{\infty} I_{xmn}f_{xmn}(\theta,\varphi). \quad (4)$$

The mode function $f_{xmn}(\theta,\varphi)$ is expressed by

$$\begin{aligned}f_{xmn}(\theta,\varphi) = {} & \mathrm{sinc}(m\pi + N_x\pi\sin\theta\cos\varphi) \\ & \times \mathrm{sinc}\left(n\pi + N_y\pi\sin\theta\sin\varphi\right) \quad (5)\end{aligned}$$

which describes a beam in the space with its peak at the direction of $(\theta_{mn},\varphi_{mn})$ and $(\pi-\theta_{mn},\varphi_{mn})$, symmetrically located in the two sides of the source plane generally. In particular, two peak directions will coincide if $\theta_{mn} = \frac{\pi}{2}$ for another kind of modes what we called end-fire modes. The peak directions satisfy

$$\begin{cases}N_x\pi\sin\theta_{mn}\cos\varphi_{mn} + m\pi = 0 \\ N_y\pi\sin\theta_{mn}\sin\varphi_{mn} + n\pi = 0\end{cases} \quad (6)$$

The wavevector of the $mn$-th mode at its peak direction can be found from as

$$\begin{cases} k_{xmn} = k\sin\theta_{mn}\cos\varphi_{mn} = \frac{-km}{N_x} \\ k_{ymn} = k\sin\theta_{mn}\sin\varphi_{mn} = \frac{-kn}{N_y} \\ k_{zmn} = \pm k\sqrt{1-\left(\frac{m}{N_x}\right)^2-\left(n/N_y\right)^2} \end{cases} \tag{7}$$

For the sake of convenience, we define a set of integer pairs as:

$$\mathbb{P} = \left\{(m,n)\in\mathbb{Z}^2 : (m/N_x)^2+\left(n/N_y\right)^2 \le 1\right\}. \tag{8}$$

If $(m,n)\in\mathbb{P}$, the corresponding mode is a propagation mode in $\pm z$ direction which can propagate away from the source and contribute significantly to the far-field. Otherwise, the mode is an evanescent one and generally contributes little to the far-field. A typical constellation of the propagation group in k-space is shown in Fig. 1(b), where each circle denotes a normalized wavevector of a propagation mode. In general, for a propagation mode, its two wave vectors are symmetrically mirrored with respect to the $k_z = 0$ plane. In particular, the two wavevectors coincide if they fall on the $k_z = 0$ plane, corresponding to the end-fire mode. It is obvious that the contribution of the propagation modes is more significant than that of the evanescent modes. Each propagation mode, as characterized by its mode function $f_{xmn}(\theta,\varphi)$, makes the most significant contribution to the far-fields at its peak directions. Since the information of far-fields predominantly concentrates within the main lobe of the propagation modes, we directly sample at the peak directions. In other words, we directly sample on the constellation. Assuming that $N_m$ denotes the total number of the modes and $N_a$ represents the number of the sampling points, we rearrange the modes and sampling points accordingly and convert into a matrix equation:

$$\overline{\mathbf{H}}\cdot\mathbf{I} = \mathbf{F} \tag{9}$$

where $\mathbf{I} = [I_1, I_2, \ldots, I_{N_m}]^T$ is the column vector containing the expansion coefficients of the current source, $\mathbf{F} = [F_x(\theta_1,\varphi_1), F_x(\theta_2,\varphi_2), \ldots, F_x(\theta_{N_a},\varphi_{N_a})]^T$is the column vector corresponding to the far-field, the upper script "$T$" means transpose. $\overline{\mathbf{H}}$ is the transfer matrix connecting the current source and it's far-field with size of $N_a \times N_m$. The entries of $\overline{\mathbf{H}}$ is respectively expressed as:

$$H(u,v) = D_x D_y\sqrt{1-\sin^2\theta_u\cos^2\varphi_u} f_v(\theta_u,\varphi_u) \tag{10}$$

where $u = 1, 2, \ldots, N_a,\quad v = 1, 2, \ldots, N_m$.

Based on SVD, the transfer matrix is decomposed into a superposition of individual singular state subspaces,

$$\overline{\mathbf{H}} = \overline{\mathbf{U}}\,\overline{\mathbf{S}}\,\overline{\mathbf{V}}^*. \tag{11}$$

where $\overline{\mathbf{U}}$ is of size $N_a \times N_a$ and is composed of orthonormal left singular vectors, $\overline{\mathbf{V}}$ is of size $N_m \times N_m$ and is composed of orthonormal right singular vectors, $\overline{\mathbf{S}}$ is of size $N_a \times N_m$ with the diagonal terms being singular values that are placed in non-increasing order. For the sake of brevity, we define a singular state for a singular value, associating with a singular state current described by the singular vector, and a singular state far field generated by the singular state current.

Since we have performed SVD for the whole system and all the singular values are all available, it is efficient to use for calculating the reconstructed current coefficient vector $\mathbf{I}_{rec}$ corresponding to the selected part of the singular values.

$$\mathbf{I}_{rec} = \sum_{j=1}^{N_s}\frac{\mathbf{U}_j^*\cdot\mathbf{F}}{s_j}\mathbf{V}_j \tag{12}$$

where $\mathbf{U}_j$, $\mathbf{V}_j$denote the $j$-th column of matrix $\overline{\mathbf{U}}$ and $\overline{\mathbf{V}}$ respectively, and $s_j$ denotes the $j$-th singular value. $N_s$ represents the number of the selected singular states. For example, when we reconstruct the common mode current, $N_s$ corresponds to the number of the common modes.

By comparing the preset current coefficient vector with the reconstructed current coefficient vector, the relative error serves as a criterion for evaluating the suitability of ENDF. The relative error is defined as:

$$Err = 20\log\left(\frac{\sqrt{\sum_{n=1}^{N_p}\left|I_n^{rec}-I_n\right|^2}}{\sqrt{\sum_{n=1}^{N_p}|I_n|^2}}\right) \tag{13}$$

where $N_p$ is the number of the propagation modes. $I_n$ denotes the preset current coefficient of the $n$-th mode. $I_n^{rec}$ is the reconstructed current coefficient of the $n$-th mode.

## III. THE ENDF OF FAR-FIELD OF CURRENT SHEETS

It is a very important issue to estimate how many independent information are included in the far fields generated by sources within a bounded region under certain noise level in the environment. As a matter of fact, it is difficult to give a clear definition for the NDF of the far-fields. However, the addition of external noise and specific techniques such as SVD may provide a kind of criterion for evaluating the ENDF which is a commonly used parameter for this purpose. We add additive white Gaussian noise (AWGN) to the far-field to simulate external noises.

### A. ENDF OF ONE CURRENT SHEET

Fig. 2(a) shows the preset current distribution of a $4\lambda \times 4\lambda$ current sheet and Fig. 2(b) shows the normalized singular values of it. According to the constellation, $N_a$=94. Three cases are calculated, all of which include all propagation modes, as well as a varying number of evanescent modes. The effect of the evanescent modes can be taken into account in the analysis. The singular values initially exhibit a gradual change and then sharply decrease after reaching a specific point referred to as the knee. We take the number of the modes corresponding to the knee as the ENDF. By sampling on the constellation, the knees of the singular values can be clearly identified and it is convenient for us to evaluate the ENDF of the far fields. The same trend in the three cases indicating that the influence of evanescent modes on the ENDF is neglected. We have shown that they can be dropped

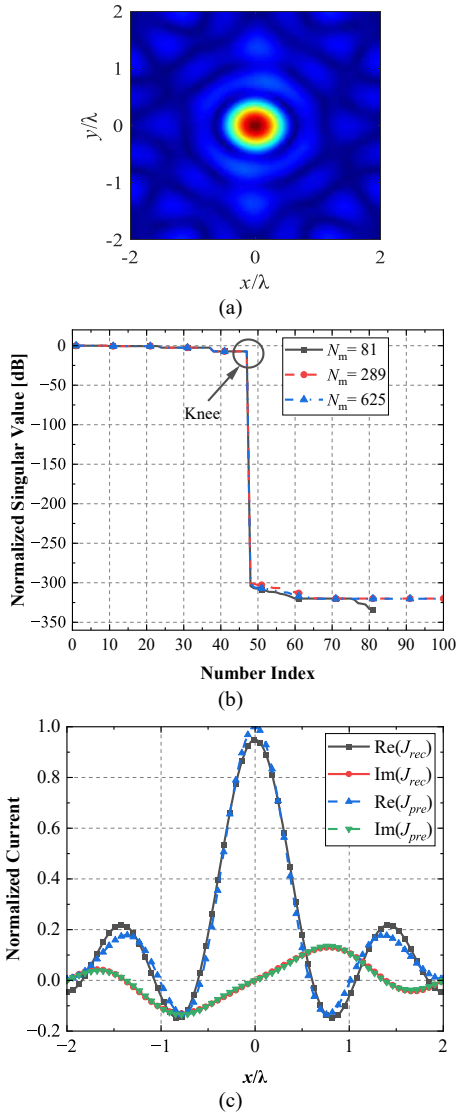


**FIGURE 2.** One current sheet. (a) Current distribution. (b) The normalized singular values. (c) Comparison between the normalized reconstructed current and the preset current on the middle line of the current sheet in the *x*-direction.

in practical systems because their contributions to the far fields are much less significant than the propagation modes.

However, at least we have to take into account all the propagation modes, and the size of the transfer matrix cannot be further shrunk. Otherwise, part of the information in the far-fields will be lost, resulting in the current cannot be accurately reconstructed. As a result, the optimal choice for $N_m$ is to include only all propagation modes considering computational costs.

We add external noise with a SNR of 30 dB to the far-fields. The reconstructed current and the preset current are depicted in Fig. 2(c), where $J_{rec}$ represents the reconstructed current and $J_{pre}$ represents the preset current. Note that both the $J_{pre}$ and the $J_{rec}$ are normalized with the peak value of the preset current amplitude. Results show that the reconstructed current obtained with the singular states in ENDF match well with the preset current.

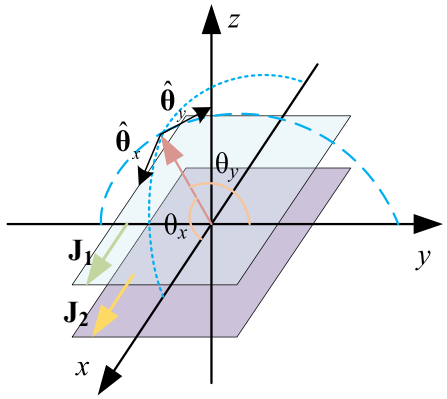


**FIGURE 3.** Two current sheets and the unit vectors in the coordinate system.

The upper limit to the available ENDF is determined by the cardinality of $\overline{\mathbf{H}}$. It can be computed by counting the number of lattice points falling into the constellation shown in Fig. 1(b). The Lebesgue measure [26] of the set $\mathbb{P}$ provides an estimate for the ENDF with high-accuracy,

$$|\mathbb{P}| \approx \frac{2\pi}{\sqrt{4ac}} \tag{14}$$

here, $a = \frac{1}{N_x^2}$ and $c = \frac{1}{N_y^2}$. Substituting them into, we can get the ENDF for the far-field of one current sheet as

$$ENDF_1 = |\mathbb{P}| \approx \frac{\pi}{\lambda^2} D_x D_y \tag{15}$$

where subscript "1" indicates that the computed results correspond to the case of one layer. It implies that the ENDF is directly proportional to the area of the current sheet, which is consistent with the [25].

### B. ENDF OF TWO PARALLEL CURRENT SHEETS

To provide a useful reference index for synthesis of non-mirror-symmetrical far-field patterns and reconstruction of the radiating parts of current sources, the case involving two parallel current sheets is investigated. Consider the two parallel current sheets shown in Fig. 3. Both sheets are rectangularly shaped with the same size. The center of the upper current sheet locates at $(0, 0, d)$, while that of the lower current sheet locates at $(0, 0, -d)$. Similar to the case of one current sheet, the normalized far-field corresponding to the $x$-polarization can be expressed as

$$F_x(\theta, \varphi) = D_x D_y \sin\theta_x \sum_{m=-\infty}^{\infty} \sum_{n=-\infty}^{\infty} \left( I_{1xmn} e^{jk_z d} + I_{2xmn} e^{-jk_z d} \right) \times f_{xmn}(\theta, \varphi). \tag{16}$$

As discussed in [24], an important issue is the impact of the distance between the two current sheets. We want to reveal the independent information that can be possibly carried in the far fields when the sizes of the two sheets and the distance between them are specified, with arbitrary current distributions on the two sheets, we consider all current distribution in the function space defined on the two sheets.

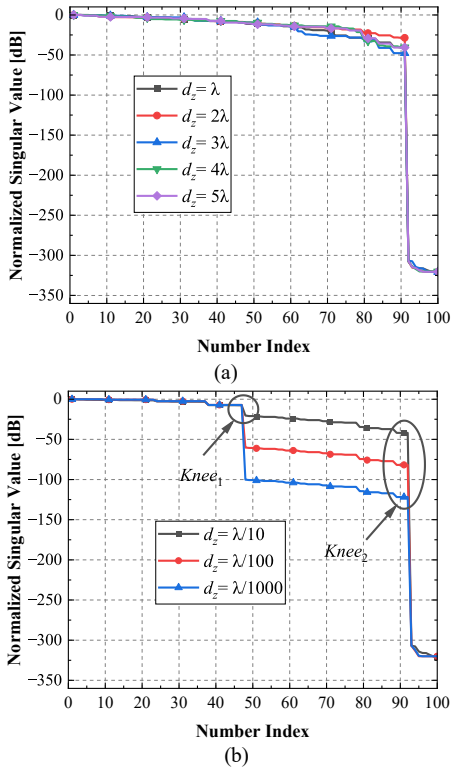


**FIGURE 4.** The normalized singular values of the channel matrix for two current sheets in parallel with different distance. (a) The distance is larger than one wavelength. (b) The distance is less than one wavelength.

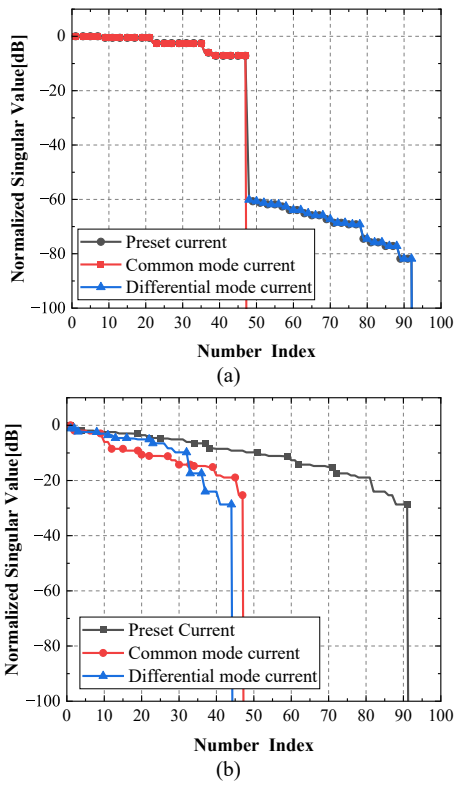


**FIGURE 5.** The normalized singular values of all mode currents, common mode currents, and differential mode currents for (a) distances smaller than the critical distance, and (b) distances larger than the critical distance.

The scenario involving a relatively large distance between two current sheets is initially investigated. Considering the case where the distance $d_z$ is larger than one wavelength, the distribution of singular values for $4\lambda \times 4\lambda$ current sheets is illustrated in Fig. 4(a). Since the phase factor term $e^{jk_z d}$ in the $z$-direction of two layers are the same for the end-fire modes, the end-fire modes need to be removed from ENDF. Let $N_e$ denote the number of the end-fire modes. $N_e = 4$ for the case where the size of the current sheet is $4\lambda \times 4\lambda$. The total ENDF can be summarized as

$$ENDF_2 = 2|\mathbb{P}| - N_e \approx \frac{2\pi}{\lambda^2} D_x D_y - N_e. \tag{17}$$

where subscript "2" indicates that the computed results correspond to the case of two layers for the larger distance.

Fig. 4(b) shows the normalized singular values when the distance $d_z$ between two current sheets is $\frac{\lambda}{10}$, $\frac{\lambda}{100}$, and $\frac{\lambda}{1000}$, respectively. Evidently, if the two current sheets are close enough, two prominent knees appear and separate the singular value curve into three segments in Fig. 4(b). Assuming that the first knee appears at $Knee_1$ and the second knee is observed at $Knee_2$. For convenience, we term the distance between the two sheets as the critical distance at which the drop at $Knee_1$ clearly appears.

Further investigation categorizes singular values into three groups, aligned with three singular value segments. The first group corresponds to the segment before the first knee, representing the singular states of the common mode currents of the two current sheets, as illustrated in Fig. 5(a). Common mode states, with the largest singular values, significantly impact the far-field. The second group lies between the two knees, representing the singular states of the differential mode currents, as depicted in Fig. 5(a). Their influence on the far fields depends on the distance of the two current sheets. The third group, after the second knee, has significantly smaller singular values than the first two groups, indicating negligible impact on the far fields. This group contains the states that are not significant to the reconstruction process.

If the distance between the two current sheets is larger than the critical distance, the corresponding normalized singular values are shown in Fig. 5(b). In this case, the singular values of the common mode states and that of differential mode states are mixed together, indicating that their contributions to the far-field are comparable.

Fig. 6 displays the preset current distribution of the two current sheets. It can be decomposed into the common mode component $J_{com}$ and the differential mode component $J_{dif}$, as shown in Fig. 7(a) and Fig. 7(b) respectively. If the distance is smaller than the critical distance, the singular state fields in the first group can be directly used to reconstruct the common mode current of the two current sheets, while the singular state fields in the second group can be utilized to reconstruct the differential mode current. Assume that $d_z = \frac{\lambda}{100}$ which is smaller than the critical distance and there is no external noise. The first singular group and the second

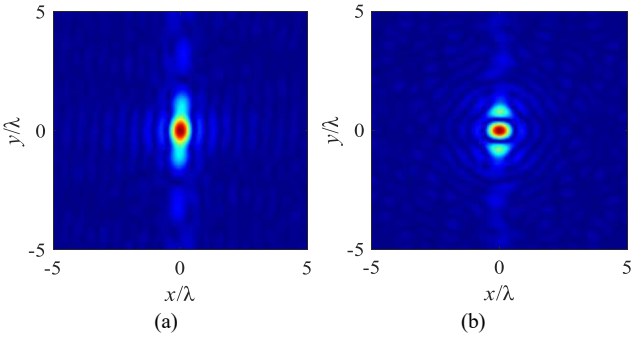


**FIGURE 6.** Current distributions. (a) Upper current sheet. (b) Lower current sheet.

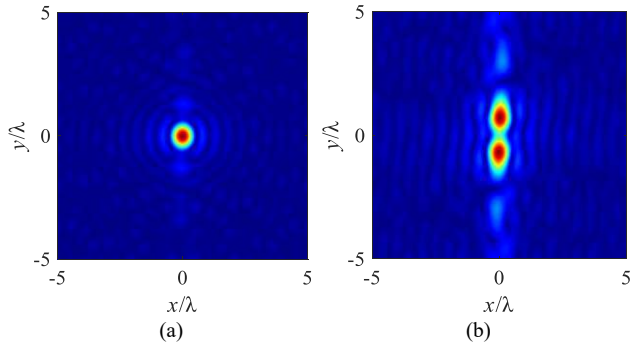


**FIGURE 7.** Preset current distributions. (a) common mode component. (b) differential mode component.

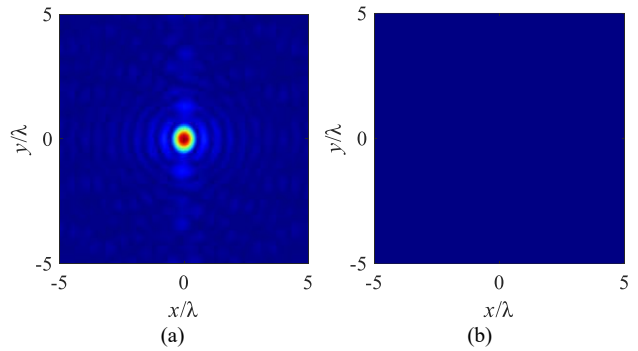


**FIGURE 8.** Reconstructed current distributions with the first singular group for (a) common mode component and (b) differential mode component.

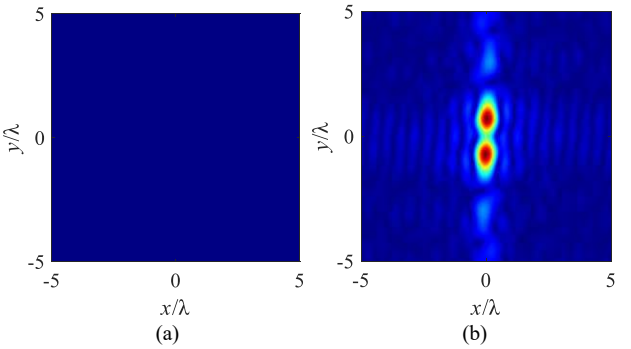


**FIGURE 9.** Reconstructed current distributions with the second singular group for (a) common mode component and (b) differential mode component.

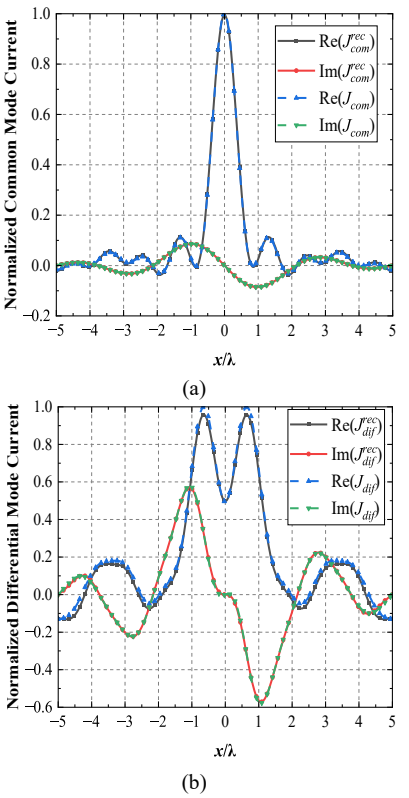


**FIGURE 10.** Comparison between normalized preset current and normalized reconstructed current on the middle line in the *x*-direction of the upper current sheet. (a) Common mode component. (b) Differential mode component.

singular group are used to reconstruct the common mode current and the differential mode current respectively, the results are shown in Fig. 8 and Fig. 9. It further confirms our view that the first singular group can be used to reconstruct the common mode current and the second singular group can be used to reconstruct the differential mode current.

To further examine the difference between the reconstructed current distribution and the preset current distribution for both common mode component and differential mode component, we only plotted the current distribution on the middle line in the $x$ direction. The results for the upper layer are shown in Fig. 10, and the results for the lower layer are shown in Fig. 11 where the reconstructed common current is denoted by $J_{com}^{rec}$ and the reconstructed differential current is denoted by $J_{dif}^{rec}$. The results show that the accuracy of reconstruction of common mode current is slightly higher than that of differential mode current.

The relative errors of the reconstructed current with different SNRs are shown in Fig. 12. Relative errors of the common mode currents and that of the differential mode currents remain consistent regardless of the proximity between the current sheets without noise. With noise present, the relative errors of the common mode currents remain relatively stable as the distance decreases, while the relative errors of the differential mode currents significantly increase. This phenomenon is due to the smaller singular values of the differential mode currents as the distance decrease, resulting

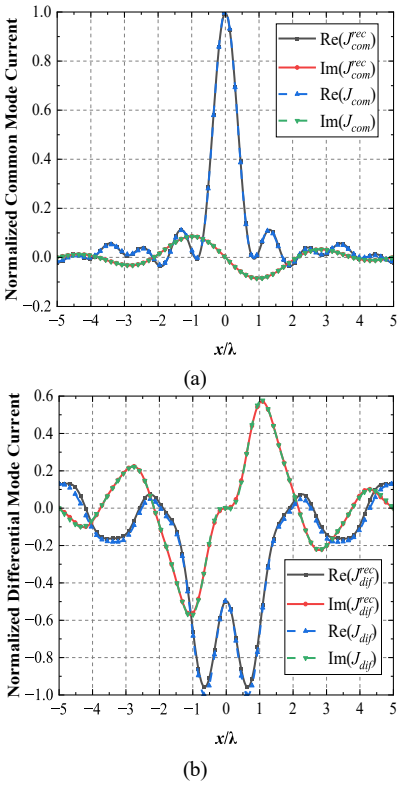


**FIGURE 11.** Comparison between normalized preset current and normalized reconstructed current on the middle line in the *x*-direction of the lower current sheet. (a) Common modes component. (b) Differential modes component.

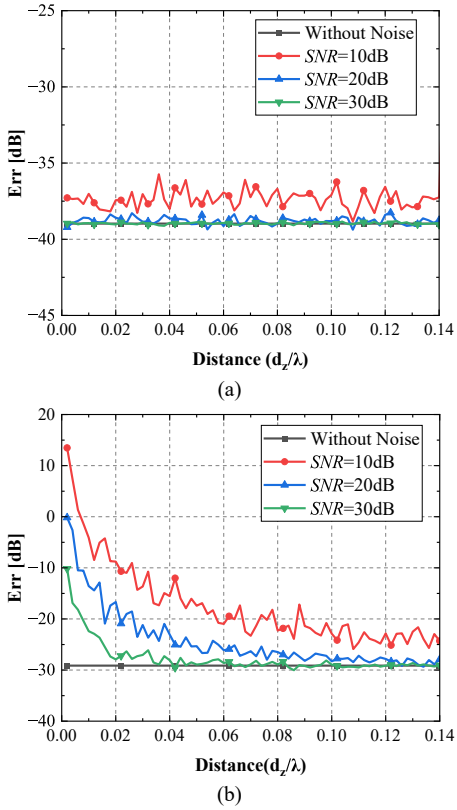


**FIGURE 12.** Relative error. (a) Relative error of common mode current at different noise levels (b) Relative error of differential mode current at different noise levels.

in a weaker intensity compared to the noises. As a result, the differential mode fields are overwhelmed by the noises and the differential mode currents cannot be accurately reconstructed. Because the amplitude of the differential mode signal is equal and the phase is opposite, as the distance between two current sheets decreases, the superposition far-fields generated by the differential mode currents of the two current sheets is extremely small, so it is easy to be overwhelmed by noises. In close proximity of the two sheets, the ENDF should contain only the common modes and exclude the differential modes.

It can be clearly demonstrated with our methods that the fields from the differential modes can be covered by noises and the ENDF will be halved, which has not been clearly revealed in [25] and other published papers. It is difficult to give an explicit criterion to judge whether the differential modes should be included in determining the ENDF of the far fields. In a noise environment with given SNR, the reconstruction error of the differential mode current is a reliable indicator for judging the influence of the differential mode field on the ENDF. However, it may be more convenient to use the knees of the singular value curves directly without performing current reconstruction. We denote the singular value drop at $Knee_1$ corresponding to a specified reconstruction error under a given SNR as the threshold. If the singular value drop exceeds the threshold, it implies that the differential modes are submerged in the noise. Thus, the ENDF is equal to the number of the common modes. Otherwise, the ENDF is calculated by, which includes the contribution from the common modes and the differential modes.

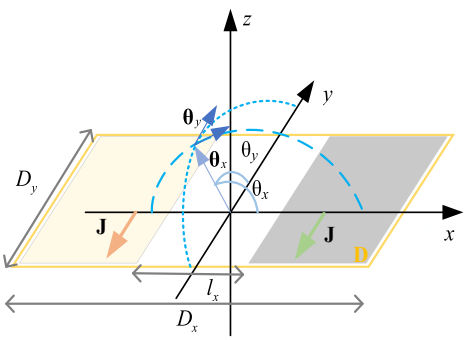


**FIGURE 13.** Two current sheets arranged in the x-axis and the unit vectors in the coordinate system.

### C. ENDF OF TWO CURRENT SHEETS IN THE SAME PLANE

The case where two current sheets lie on the same plane is studied since it is more of a common interest in antenna array configurations. Two rectangular current sheets are located in the same plane with a spacing $l_x$ between the edges, as illustrated in Fig. 13. Here $D_x = M\lambda$, $D_y = N\lambda$, $l_x = M_0\lambda$, and $M$, $N$, $L$ are all integers. The total area of the two

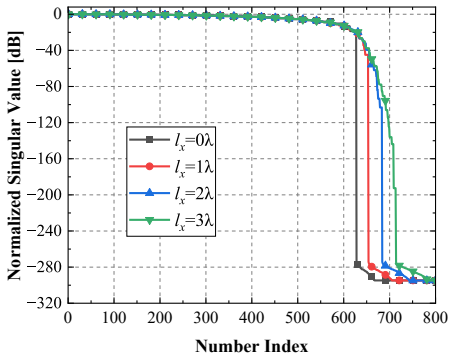


**FIGURE 14.** The normalized singular values of two current sheets with size 10λ × 10λ in the same plane for different spacings $l_x$.

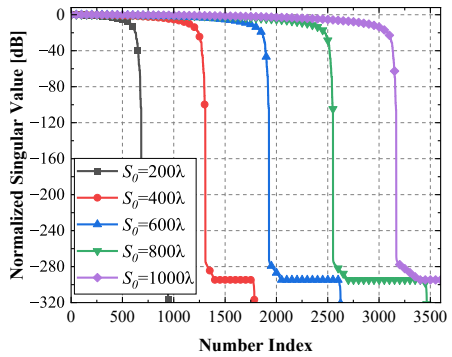


**FIGURE 15.** The normalized singular values of two current sheets with spacing equal to 2λ in the same plane for different area $S_0$.

current sheets is $S_0 = (M - M_0) \times N\lambda^2$. Considering only $x$-polarization, its far-field can be represented as

$$F_x(\theta, \varphi) = \sin\theta_x \int_{\frac{l_x}{2}}^{\frac{D_x}{2}} \int_{-\frac{D_y}{2}}^{\frac{D_y}{2}} e^{jk_x x + jk_y y} I_x(x, y) dy dx + \sin\theta_x \int_{-\frac{D_x}{2}}^{\frac{-l_x}{2}} \int_{-\frac{D_y}{2}}^{\frac{D_y}{2}} e^{jk_x x + jk_y y} I_x(x, y) dy dx \quad (18)$$

Note that the integration area covers the two sheets. The influence of the distance between the two current sheets in the same plane on the ENDF is investigated, and the results are illustrated in Fig. 14. Obviously, when the sizes of the two current sheets are fixed, the distance between them increases, the ENDF remains nearly unchanged. This indicates that the spacing between the two current sheets has little impact on the ENDF if two current sheets are in the same plane. Fig. 15 shows the normalized singular values of the fixed spacing $l_x$ for different area $S_0$, as mentioned in the results for one single current sheet, the ENDF for two current sheets in the same plane is directly proportional to the area of the region containing the current.

## IV. CONCLUSION

This paper calculates ENDF of the far-fields generated by current sheets under certain noise level in free space by directly sampling on constellation. It is known that the pattern of a single current sheet is symmetrical to the source plane. In order to realize a non-mirror symmetrical pattern, we may have to use two current-sheets. Therefore, this paper focuses on the ENDF of the far fields generated by two planar current sheets, as is known the ENDF keeps almost unchanged if more than two sheets are used. It is demonstrated with our methods that the fields from the differential modes can be covered by noises and the ENDF will be halved when two parallel sheets are very close to each other, which has not been revealed in other published papers.

These findings can be applied in antenna synthesis and reconstructing sources from far fields and may provide us an effective estimate parameter for synthesis of planar antenna arrays with non-mirror symmetrical radiation patterns. For example, the results may be applied for reconstructing surface current on the two sides of an object from the far fields. It can provide us a useful criterion for determining some of the main parameters of the radiation pattern that can be realized with sources in a certain region; or for determining to what extent the sources can be reconstructed from the electromagnetic fields outside the source region. Meanwhile, it may have potential applications in computational electromagnetics such as in the analysis of very thin plates using the method of moment in conjunction with surface integral equation, as it is clearly indicated that only common modes are significant in these situations.

## REFERENCES

[1] G. Leone, F. Munno, and R. Pierri, "Synthesis of angle arrays by the NDF of the radiation integral," *IEEE Trans. Antennas Propag.*, vol. 69, no. 4, pp. 2092–2102, Apr. 2021.

[2] J.-C. Bolomey, O. M. Bucci, L. Casavola, G. D'Elia, M. D. Migliore, and A. Ziyyat, "Reduction of truncation error in near-field measurements of antennas of base-station mobile communication systems," *IEEE Trans. Antennas Propag.*, vol. 52, no. 2, pp. 593–602, Feb. 2004.

[3] B. Stupfel and S. Vermersch, "Plane-wave synthesis by an antenna-array and RCS determination: Theoretical approach and numerical simulations," *IEEE Trans. Antennas Propag.*, vol. 52, no. 11, pp. 3086–3095, Nov. 2004.

[4] M. D. Migliore, "Minimum trace norm regularization (MTNR) in electromagnetic inverse problems," *IEEE Trans. Antennas Propag.*, vol. 64, no. 2, pp. 630–639, Feb. 2016.

[5] G. Leone, F. Munno, and R. Pierri, "Inverse source on conformal conic geometries," *IEEE Trans. Antennas Propag.*, vol. 69, no. 3, pp. 1596–1609, Mar. 2021.

[6] R. Solimene, M. A. Maisto, and R. Pierri, "Inverse source in the presence of a reflecting plane for the strip case," *J. Opt. Soc. Amer. A, Opt. Image Sci.*, vol. 31, no. 12, pp. 2814–2820, Dec. 2014.

[7] Z. Lin, R. Guo, M. Li, F. Yang, S. Xu, and A. Abubakar, "Study on the degrees of freedom of scattered fields in nonlinear inverse scattering problems," in *Proc. IEEE Int. Symp. Antennas Propag. USNC-URSI Radio Sci. Meet. (APS/URSI)*, 2021, pp. 1845–1846.

[8] R. Solimene, M. A. Maisto, and R. Pierri, "Inverse scattering in the presence of a reflecting plane," *J. Opt.*, vol. 18, no. 2, 2016, Art. no. 025603.

[9] O. M. Bucci and T. Isernia, "Electromagnetic inverse scattering: Retrievable information and measurement strategies," *Radio Sci.*, vol. 32, no. 6, pp. 2123–2137, Nov./Dec. 1997.

[10] A. Pizzo, T. L. Marzetta, and L. Sanguinetti, "Spatially-stationary model for holographic MIMO small-scale fading," *IEEE J. Sel. Areas Commun.*, vol. 38, no. 9, pp. 1964–1979, Sep. 2020.

[11] M. D. Migliore, "On the role of the number of degrees of freedom of the field in MIMO channels," *IEEE Trans. Antennas Propag.*, vol. 54, no. 2, pp. 620–628, Feb. 2006.
[12] K. Haneda et al., "Measurement-based analysis of spatial degrees of freedom in multipath propagation channels," *IEEE Trans. Antennas Propag.*, vol. 61, no. 2, pp. 890–900, Feb. 2013.
[13] A. S. Y. Poon, R. W. Brodersen, and D. N. C. Tse, "Degrees of freedom in multiple-antenna channels: A signal space approach," *IEEE Trans. Inf. Theory*, vol. 51, no. 2, pp. 523–536, Feb. 2005.
[14] G. T. Di Francia, "Degrees of freedom of an image," *J. Opt. Soc. Am.*, vol. 59, pp. 799–804, Jul. 1969.
[15] M. Bendinelli, A. Consortini, L. Ronchi, and B. R. Frieden, "Degrees of freedom, and eigenfunctions, for the noisy image," *J. Opt. Soc. Am.*, vol. 64, pp. 1498–1502, Nov. 1974.
[16] S. S. A. Yuan, Z. He, X. Chen, C. Huang, and W. E. I. Sha, "Electromagnetic effective degree of freedom of an MIMO system in free space," *IEEE Antennas Wireless Propag. Lett.*, vol. 21, no. 3, pp. 446–450, Mar. 2022.
[17] R. Li et al., "An electromagnetic information theory based model for efficient characterization of MIMO systems in complex space," *IEEE Trans. Antennas Propag.*, vol. 71, no. 4, pp. 3497–3508, Apr. 2023.
[18] M. D. Migliore, "Horse (electromagnetics) is more important than horseman (information) for wireless transmission," *IEEE Trans. Antennas Propag.*, vol. 67, no. 4, pp. 2046–2055, Apr. 2019.
[19] R. Piestun and D. A. B. Miller, "Electromagnetic degrees of freedom of an optical system," *J. Opt. Soc. Amer. A*, vol. 17, pp. 892–902, May 2000.
[20] L. W. Hanlen and M. Fu, "Wireless communications systems with spatial diversity: A volumetric approach," in *Proc. IEEE Int. Conf. Commun.*, 2003, pp. 2673–2677.
[21] J. Xu and R. Janaswamy, "Electromagnetic degrees of freedom in 2-D scattering environments," *IEEE Trans. Antennas Propag.*, vol. 54, no. 12, pp. 3882–3894, Dec. 2006.
[22] G. B. Xiao and R. Liu, "Direct method for reconstructing the radiating part of a planar source from its far-fields," *Electronics*, vol. 11, p. 3852, Nov. 2022.
[23] G. Xiao, X. Wang, and T. Zang, "Optimization of far-field patterns based on direct synthesis results," *IEEE Trans. Antennas Propag.*, vol. 71, no. 12, pp. 9956–9961, Dec. 2023, doi: 10.1109/TAP.2023.3321429.
[24] G. B. Xiao, T. Zang, and R. Liu. "Synthesis of non-mirror-symmetrical far-field patterns using two parallel current sheets," *Electronics*, vol. 12, p. 892, Feb. 2023.
[25] A. Pizzo, T. L. Marzetta, and L. Sanguinetti, "Degrees of freedom of holographic MIMO channels," in *Proc. IEEE 21st Int. Workshop Signal Process. Adv. Wireless Commun. (SPAWC)*, 2020, pp. 1–5.
[26] W. G. Nowak, "Primitive lattice points inside an ellipse," *Czechoslovak Math. J.*, vol. 55, pp. 519–530, Jun. 2005.